INTERNAL REPORT

K-band System Temperature Forecast for the Sardinia Radio Telescope

F. Buffa[1], G. Serra[1], P. Bolli[2], A. Fara[1], G.L. Deiana[1], F. Nasir[3], C. Castiglia[3], A.M.S. Delitala[3]

[1]INAF - Osservatorio Astronomico di Cagliari, via della Scienza 5, Selargius (CA), Italy
[2]INAF - Osservatorio Astrofisico di Arcetri, largo Enrico Fermi 5, Firenze, Italy
[3]Arpas - Dipartimento Meteoclimatico, viale Porto Torres, Sassari, Italy

Report N. 54, Released: 07/04/2016
Reviewer: E. Carretti

OAC Osservatorio Astronomico di Cagliari

1 Introduction

The Sardinia Radio Telescope (SRT) has been designed with the aim of achieving high scientific standards and high productivity. At the higher frequencies the best performances can be obtained if the external error sources affecting the radio astronomical signal are monitored and mitigated. In this context, thermal and gravitational deformations must be measured in real-time and corrected by the active optical system, RFI sources must be continuously detected, classified and possibly mitigated. Finally, the atmosphere variability must be carefully monitored.
It is well known that the atmosphere starts strongly interacting with the incoming radio astrononical signal around 22 GHz, i.e. where the first resonance frequency of the H_2O occurs. For such a reason, a modern radio astronomical facility should be equipped with an efficient atmosphere monitoring system. To this purpose, a microwave radiometer[1] is operating at the SRT site, allowing the astronomers a real-time monitoring of the atmosphere during the K-band surveys (from 18 to 26 GHz, at the moment the SRT maximum observation frequency). The radiometer provides the sky opacity and other important parameters useful to calibrate the astronomical observations and to retrieve the atmosphere status. However, an efficient exploitation of a radio telescope needs also a reliable weather model able to forecast the local variations of the atmospheric conditions.
In this report we develop and assess the effectiveness of a procedure, based on a numerical weather model, to predict both the atmosphere opacity and the antenna system temperature (T_{SYS}) several hours before a radio astronomical survey. Therefore, it can give the opportunity to dynamically schedule the "best experiment" with respect to the predicted atmosphere status.
Basically, the procedure, outlined in Fig. 1, calculates the T_{SYS} in three different ways. The first two follow the Cortés Medellín's approach [1, 2], requiring an accurate model of the antenna radiation pattern. One uses as input the radiosounding (RDS) data, measured daily at the Decimomannu airport[2], the other one the weather forecast model (WRF) data coming daily from the Sardinia Department for the hydro-weather forecast (ARPAS) (Section 2.1). The third way follows a simplified approach, but not less accurate than the previous one, since it exploits the zenith opacity data measured by the SRT radiometer (RDM) (Section 2.2).
RDS or WRF data set are needed to calculate first the molecular absorption coefficients, then the sky opacity and T_{SYS} (Section 3).
It is worth noting that the WRF data are the outputs of a state-of-art weather model, developed for the regional forecast weather, able to predict the molecular species concentration in the atmosphere above Sardinia up to 36 hours in advance. How the procedure makes use of the WRF data is described in Section 4. Finally, in order to validate the T_{SYS} forecast procedure, comparisons with T_{SYS} measured with skydip[3] taken with the SRT were done and described in Section 5.

2 System Temperature Model

The antenna system temperature may be modeled for a given frequency provided that the atmosphere parameters and the antenna radiation pattern are known. The formalism described in this section derives from [1], where a unique model for the SKA project is proposed. The same approach has been applied also to Basic Element for SKA Training [2].
The Matlab code described in [2] has been here totally revised, first by using a full vectorized approach to reduce the computation time of the calculations, then by making it compatible with the weather model forecast code.

[1] Radiometrics M-3000A.

[2] Two launches per day are performed at the Decimomannu air force base (LIED) about 28 km far from SRT site.

[3] The skydip is an observation strategy commonly used in astronomical data calibration.

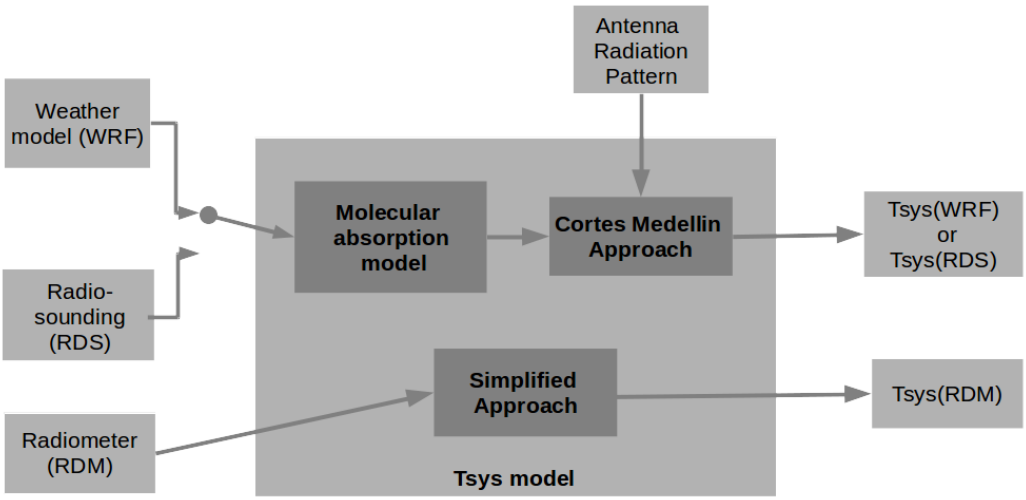

Figure 1: Blocks diagram of the procedure. Weather forecast model (WRF) and radiosounding (RDS) data are used to predict the T_{SYS} with a molecular absorption model and the Cortés Medellín's approach. This is a rigourous approach that, however, requires the antenna radiation pattern. T_{SYS} can also be calculated from radiometer (RDM) data following a simplified approach which merely considers only the antenna main beam.

2.1 Precise T_{SYS} Estimate

An antenna pointing to the direction $\mathbf{r}_o$ with a cold sky will produce a system temperature [1]

$$T_{SYS} = \eta_L T_A + (1 - \eta_L) T_p + T_{REC} \tag{1}$$

$$T_A(\nu|\mathbf{r}_o) = \frac{\iint_{4\pi} T_b(\nu, \theta', \phi') P_n(\nu, \theta, \phi) \sin\theta \, d\theta \, d\phi}{\iint_{4\pi} P_n(\nu, \theta, \phi) \sin\theta \, d\theta \, d\phi} \tag{2}$$

where

- $\mathbf{r}_o$: antenna pointing direction defined by the coordinates $(\theta_o, \phi_o, \delta_o)$, i.e. co-elevation, azimuth angle and rotation angle of the antenna system around the antenna axis, respectively (see Fig. 2);
- η_L: antenna radiation efficiency depending on ohmic losses, commonly assumed to be close to one;
- T_A: antenna noise temperature (effective atmosphere temperature);
- T_p: physical temperature of the antenna;
- T_{REC}: receiver noise temperature;
- T_b: brightness temperature;
- P_n: total radiation antenna pattern.

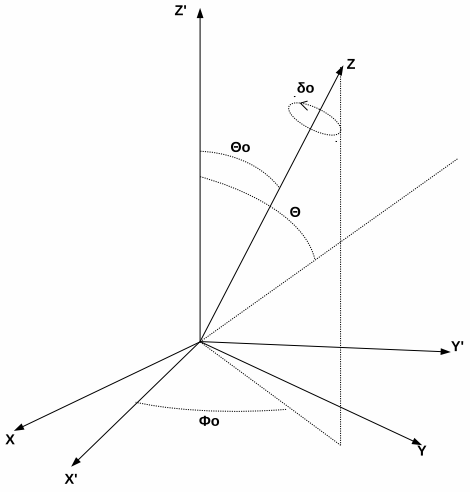

Figure 2: Coordinate systems, the Z axis represents the antenna pointing direction.

Considering Fig. 2, the following set of equations allows to express the sky reference system (θ', ϕ') with respect to the reference system on-board the antenna (θ, ϕ), given the direction of the antenna axis (θ_o, ϕ_o, δ_o) [2]

$$\begin{aligned}
\theta' &= \arccos[\sin\theta_o \sin(\theta)\sin(\phi+\delta_o) + \cos(\theta_o)\cos(\theta)] \\
\phi' &= \arctan\left[\frac{A+B-C}{D-E+F}\right] \\
A &= \sin(\phi_o)\sin(\theta_o)\sin(\phi+\delta_o) \\
B &= cos(\phi_o)cos(\phi_o)\sin(\theta)sin(\phi+\delta_o) \\
C &= \cos(\phi_o)\sin(\theta_o)\cos(\theta) \\
D &= \cos(\phi_o)\sin(\theta)\cos(\phi+\delta_o) \\
E &= \sin(\phi_o)\cos(\theta_o)\sin(\theta)\sin(\phi+\delta_o) \\
F &= \sin(\phi_o)\sin(\theta_o)\cos(\theta)
\end{aligned} \tag{3}$$

To calculate T_{SYS} with this approach, an accurate representation of P_n is required. For this reason, a 22 GHz modeling of the SRT total far-field radiation pattern (co-polar and cross-polar components) has been simulated (Fig. 3) by using GRASP[4], a popular commercial electromagnetic software suitable to calculate the field radiation pattern of reflector antennas. In our case, a GRASP project, consisting of a simplified SRT geometrical model (without quadripods) illuminated by a tabulated realistic feed positioned in the gregorian focus, was used to generate the two far-field pattern components.
A good tradeoff between the accurate representation of P_n and the simulation computation time was reached by exploiting the quasi-ϕ rotational simmetry of the SRT far-field (meaning that only few ϕ-planes are sufficient to know the whole antenna pattern). In this way, a far-field cut every 45° was calculated only in the ϕ angular quadrant from 0° to 90°. Moreover, each ϕ-cut was sampled with 501 points in the θ angular range from 0° to 1° and 501 points from 1° to 180°, so having a higher angular resolution close to the main beam, where most of the power has radiated, and a lower angular resolution in far side lobes, with a negligible

[4]http://www.ticra.com/products/software/grasp

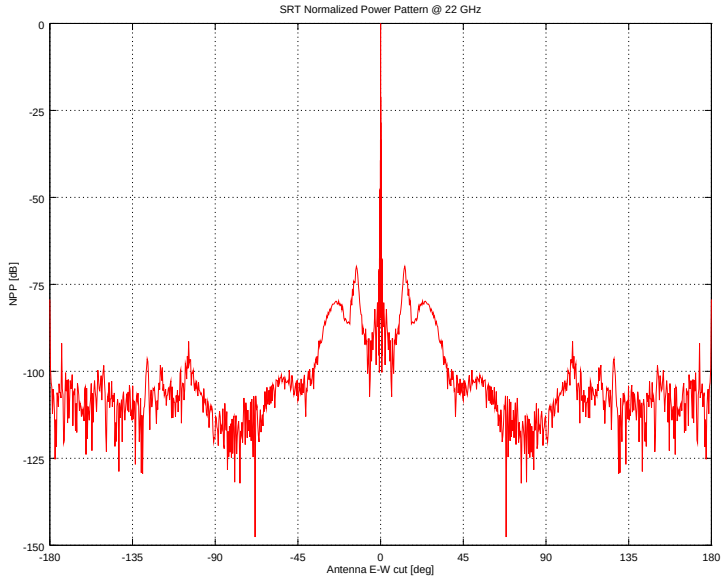

Figure 3: 22 GHz SRT radiation pattern as obtained by the GRASP simulation.

decreasing of the far-field calculation accuracy. Then, the far-field cuts of the remaining 3 quadrants were added to complete the P_n calculation by means of the matlab code, after taking into account that the cross-polar component phase changes of 180° in the symmetrical azimuth planes.
Now, assuming that sky brightness temperature is uniform, T_b may be expressed as

$$T_b^{sky}(\nu,\theta') = T_{bo}(\nu)e^{-\tau_\nu(0,s_o)} + \int_0^{s_o} \frac{\kappa_a(\nu,s)T(s)e^{-\tau_\nu(s)}}{\sqrt{1-\left(\frac{\sin(\theta')}{1+s/r_e}\right)^2}}\,ds \tag{4}$$

where

- T_{bo}: background brightness temperature;
- τ_ν: zenithal sky opacity;
- κ_a: absorption coefficient of atmospheric constituents[5];
- s_o: troposphere height;
- r_e: Earths radius;
- T: atmospheric layer temperature in degree Kelvin.

The background brightness temperature is defined as

$$T_{bo}(\nu) = T_{CBM} + T_{g_o}(\nu_o/\nu)^\beta \tag{5}$$

where T_{CBM} is the 2.73 K cosmic microwave background emission and $T_{g_o}(\nu_o/\nu)^\beta$ takes into account the galactic emission. A good parameters choice for the galactic contribution in the range $20-100$ GHz is: β=3.0, T_{g_o}=20 K and ν_o=408 MHz [1].

[5]Here the absorption coefficient κ_a is expressed in Np/km while in the following formulae it will be given in dB/km ($\kappa_a[Np/km] = \frac{1}{10\log e}\kappa_a[dB/km]$)

The sky opacity is defined as

$$\tau_\nu(s) = \int_0^s \frac{\kappa_a(\nu, s')}{\sqrt{1 - \left(\frac{\sin(\theta')}{1+s'/r_e}\right)^2}}\, ds' \tag{6}$$

Finally, taking into account the ground contribution in terms of emission and scattering, one can write

$$T_b(\nu, \theta', \phi') P_n(\nu, \theta, \phi) = \begin{cases} T_b^{sky}(\nu, \theta') P_n(\nu, \theta, \phi) & 0 \le \theta' \le \pi/2 \\ \left[\left(1 - \widetilde{\Gamma}\left(\theta_1\right)\right) T_{gnd} + \widetilde{\Gamma}\left(\theta_1\right) T_b^{sky}\left(\theta_1\right)\right] P_n(\nu, \theta, \phi) & \pi/2 < \theta' \le \pi \end{cases} \tag{7}$$

$$\widetilde{\Gamma}\left(\theta_1\right) = \frac{\Gamma_\parallel\left(\theta_1\right) + \Gamma_\perp\left(\theta_1\right)}{2} \tag{8}$$

where $\theta_1 = \pi - \theta'$, T_{gnd} is the ground temperature, and $\widetilde{\Gamma}\left(\theta_1\right)$ is the so-called "simplified" reflection coefficient obtained averaging the two, polarization dependent, power refraction coefficients at air-ground interface [1] defined by

$$\begin{aligned} \Gamma_\parallel\left(\theta_1\right) &= \left| \frac{\cos\theta_1 - \sqrt{\varepsilon - \sin^2\theta_1}}{\cos\theta_1 + \sqrt{\varepsilon - \sin^2\theta_1}} \right|^2 \\ \Gamma_\perp\left(\theta_1\right) &= \left| \frac{\varepsilon\cos\theta_1 - \sqrt{\varepsilon - \sin^2\theta_1}}{\varepsilon\cos\theta_1 + \sqrt{\varepsilon - \sin^2\theta_1}} \right|^2 \end{aligned} \tag{9}$$

where ε is the relative permittivity ($\varepsilon \approx 3.5$ for dry soil).

2.2 Approximated T_{SYS} Estimate

If an independent measurement of zenith opacity is available (e.g. from a radiometer), a very simplified formula for T_{SYS} can be used [3]

$$T_{SYS}(\theta_o) = T_{atm}\eta_f \left(1 - e^{-\tau_\nu X(\theta_o)}\right) + (1 - \eta_f) T_{gnd} + T_{REC} \tag{10}$$

where

- η_f: feed efficiency. Its value is instrinsic of each telescope feed and it has usually calculated by fitting a skydip data set. Here, we assume it equal to 0.9 and postpone the calculation of this SRT parameter to a future work;
- T_{atm}: effective temperature in atmosphere or mean radiative temperature of atmosphere;
- $X(\theta_o)$: air mass at θ_o zenith angle or co-elevation (a simple and commonly adopted air mass approximation is $X(\theta_o) = \sec\theta_o$);
- T_{gnd}: ground level temperature.

In such an approach one considers the brightness temperature T_b calculated only on the antenna main beam, without considering the spill-over effects and the contributions from the other angular directions. This approximation can be considered accurate enough for a highly directive radio telescope, as SRT, working at high frequencies (from K-band up), and, ever more so, when radiometer measurements are used.
The effective temperature T_{atm} may be regarded as the averaged atmosphere temperature weighted, for an atmosphere layer at the height s_o, by the specific contribution of each molecular species to the radiative transfer for a given frequency

$$T_{atm} = \frac{\int_0^{s_o} \kappa_a(\nu, s) T(s) e^{-\tau_\nu(s)}\, ds}{\int_0^{s_o} \kappa_a(\nu, s) e^{-\tau_\nu(s)}\, ds} \tag{11}$$

Otherwise, for optically thin channels, we can approximate T_{atm} as the average profile temperature weighted by the water vapor density, $\rho_v(s)$

$$T_{atm} \approx \frac{\int_0^{s_o} \rho_v(s) T(s)\, ds}{\int_0^{s_o} \rho_v(s)\, ds} \tag{12}$$

The evaluation of T_{atm} by (11) and (12) may be difficult if a radiosouding profile is not available. In this case, an approximate formula, valid for SRT [4] and only depending on the ground level temperature T_{gnd} may be applied

$$T_{atm} \approx 0.683\, T_{gnd} + 77.919 \tag{13}$$

3 Molecular Absorption Model

The RDS or WRF data provide the thermodynamic variables and molecular species concentration in the atmospheric layers. When these data set are available, as in our case, an absorption model can be used first to calculate the absorption coefficients for each single molecular species interacting with the incoming radiation and, then, to derive the τ_ν. It is worth noting that the τ_ν derived by (6) from RDS or WRF data might be used both in (1) and (10). In this report we decided to use τ_ν by (6) in (1), adopting (10) instead only for the radiometer opacity.
Since in the centimeter and sub-centimeter wavelength range only rotational transitions must be taken into account and only O_2 and H_2O give a remarkable contribution to the absorption [1, 5], later in the next sub-sections only the coefficients of the water vapor and liquid water [6], and oxygen [7] are considered. In addition, the same tropospheric water vapor and oxygen absorption models proposed by Cortés Medellín in [1] are here used. Actually, unlike Cortés Medellín, who describes the atmosphere as a set of static parameters representing the mid-latitude standard atmosphere, for the absorption model, here considered, a dynamic approach based on the WRF data is preferred. As a matter of fact, the WRF data allow our model to take into account even the high variability of water vapor content in the atmosphere. Unfortunately, this is not true for the RDS data, because they are are available only twice-per-day and are not enough to get the same WRF data time resolution.
Furthermore, it is well known that the frequency behaviour of the water vapor and oxygen molecules coefficients shows a superimposition of well defined spectral lines, i.e., those due to the resonance and the other one more smoothed, called continuum, which is weakly dependent on the frequency. In the absorption models, here considered, the line part and the continuum one are considered as a whole.
Finally, although the absorption spectra are dominated by the water vapor variations, the model can efficiently predict even the absorption due to the liquid water content (LWC), which may be carried by the cloud systems at different heights from the ground level to the troposphere limits.
Now, going in the analytic description of the absorption model, (14) describes, for a given molecular species and for a given frequency ν, the so-called power-absorption coefficient

$$\kappa_\nu = n\, S(T) F(\nu) \tag{14}$$

where n is the number of molecules per unit volume, i.e. the number density, $S(T)$ is the line intensity depending on the layer temperature, while $F(\nu)$ is the line shape function which can change with the temperature T and pressure P, relating in turn to the line broadening [1]. Considering the implicit dependence of T and P from hight s, the atmospheric absorption coefficient can be expressed as

$$\kappa_a(\nu, s) = \kappa^{vap}_{H_2O}(\nu, s) + \kappa^{liq}_{H_2O}(\nu, s) + \kappa_{O_2}(\nu, s) \tag{15}$$

The typical behavior of κ_a is represented in Fig. 4. The plot shows the κ_a variation with the frequency ν for a low-altitude layer with the following parameters: water vapor density = 12 g/m^3, liquid water density = 0.25 g/m^3, P = 1013 hPa, T = 300 K.

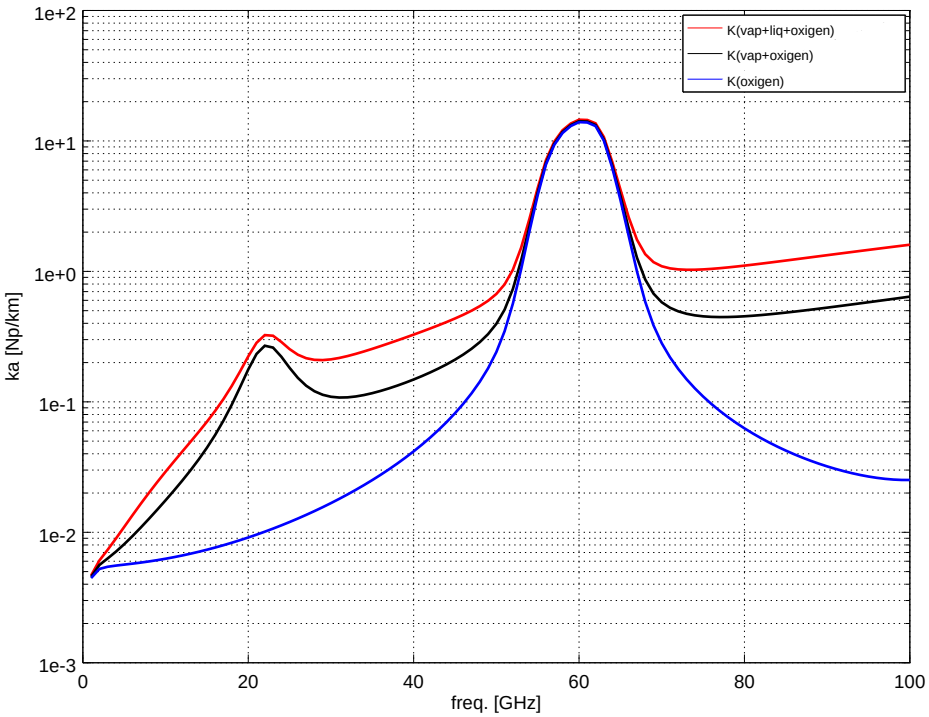

Figure 4: Frequency dependence of κ_a, the contribution of the three molecular constituents is considered: liquid + vapor + oxygen (red line), vapor + oxygen (black line) and oxygen only (blue line).

3.1 Water Vapor Absorption

With reference to Tab. 1 where all the parameters are listed, we define the water vapor absorption coefficient [6] as

$$\kappa_{H_2O}^{vap}(\nu) = 2\nu^2\rho_v \left(\frac{300}{T}\right)^{\frac{5}{2}} \sum_{i=1,i_m} A_i e^{-\mathcal{E}_i'/T} \mathcal{F}_{H_2O}(\nu,\nu_i) + \Delta\kappa(\nu) \qquad [dB/km] \tag{16}$$

where the line-shape is given by

$$\mathcal{F}_{H_2O}(\nu,\nu_i) = \frac{\gamma_i}{(\nu_i^2-\nu^2)^2 + 4\nu^2\gamma_i^2} \tag{17}$$

$$\gamma_i = \gamma_{io}\left(\frac{P}{1013}\right)\left(\frac{300}{T}\right)^{x_i}[1 + 0.01 a_i \frac{\rho_v T}{P}] \qquad [GHz] \tag{18}$$

At a given frequency ν, expressed in GHz, ρ_v represents the water vapor density in g/m^3, P is the pressure expressed in hPa and T is the temperature in K. Obviously ρ_v, P and T may (strongly) variate in time and with the layer height s. $\Delta\kappa(\nu)$ is an empirical correction term defined as

$$\Delta\kappa(\nu) = 4.69\ 10^{-6}\rho_v \left(\frac{P}{1000}\right)\left(\frac{300}{T}\right)^{2.1} \nu^2 \qquad [dB/km] \tag{19}$$

i	ν_i [GHz]	$\mathcal{E}_i'[K^{-1}]$	A_i	γ_{io} [GHz]	a_i	x_i
1	22.235150	644	1.0	2.85	1.75	0.626
2	183.31012	196	41.9	2.68	2.03	0.649
3	323.00000	1850	334.4	2.30	1.95	0.420
4	325.15380	454	115.7	3.03	1.85	0.619
5	380.19680	306	651.8	3.19	1.82	0.630
6	390.00000	2199	127.0	2.11	2.03	0.330
7	436.00000	1507	191.4	1.50	1.97	0.290
8	438.00000	1070	697.6	1.94	2.01	0.360
9	442.00000	1507	590.2	1.51	2.02	0.332
10	448.00080	412	973.1	2.47	2.19	0.510

Table 1: Water vapor absorption model parameters [6].

3.2 Liquid Water Absorption

As in the case of water vapor, the LWC has a high variability and hydrometeors (liquid water and ice particles) can play a significant role in the radiative transfer budget. A rigorous treatment should require to consider the scattering effects, but here only the absorption effects will be dealt with.
The MPM93 is an effective absorption model for suspended liquid water droplets [6]. In the MPM93 model the Rayleigh approximation is used to treat the microwaves-droplets interaction: such an approximation is valid when r $< 0.05\ \lambda$, where r is the particle radius and λ is the wavelength. For the SRT K-band (18-26 GHz), it means that r $< 830\ \mu$m @ 18 GHz, which is true for almost every aerosol and cloud classes. In fact, the mean particle radius for stratus, cumulus, and nimbus clouds is in the range of 10 $-1000\ \mu$m [5]. Under the above conditions the model validity is up to about 300 GHz.
Tab. 2 shows the characteristics of the main cloud classes in terms of LWC. It is worth noting that the different types of clouds correspond to different possible amounts of LWC.
Now, introducing $N^{''}$, the imaginary part of the complex refractivity, the liquid water absorption is formulated as

$$\kappa_{H_2O}^{liq} = 0.182\ \nu N^{''} \qquad [dB/km] \tag{20}$$

where ν is the frequency in GHz. $N^{''}$ may be expressed as

$$N^{''} = \frac{3}{2}\frac{LWC}{m}\left[\frac{3\epsilon_r^{''}}{(\epsilon_r^{'}+2)^2+(\epsilon_r^{''})^2}\right] \tag{21}$$

where $0.0 <$ LWC $< 5.0\ g/m^3$ and m is the water bulk density. For instance, in heavy fog conditions (about 50 m visibility) with droplets suspended in saturated sea level air at 30°C, LWC $\simeq 1\ g/m^3$ (the reader still considers Tab. 2 for references to the most significant cloud classes). The complex permittivity $\epsilon_r = \epsilon_r^{'} + i\epsilon_r^{''}$ may be expressed as

$$\epsilon_r^{'} = \epsilon_o - \nu^2\left[\frac{\epsilon_o-\epsilon_1}{\nu^2+\gamma_1^2}+\frac{\epsilon_1-\epsilon_2}{\nu^2+\gamma_2^2}\right] \tag{22}$$

$$\epsilon_r^{''} = \nu\left[\gamma_1\frac{\epsilon_o-\epsilon_1}{\nu^2+\gamma_1^2}+\gamma_2\frac{\epsilon_1-\epsilon_2}{\nu^2+\gamma_2^2}\right] \tag{23}$$

$$\epsilon_o = 77.66 + 103.3(\Theta - 1) \tag{24}$$

$$\epsilon_1 = 0.0671\epsilon_o \tag{25}$$

$$\epsilon_2 = 3.52 \tag{26}$$

$$\gamma_1 = 20.20 - 146(\Theta-1) + 316(\Theta-1)^2 \qquad [GHz] \tag{27}$$

$$\gamma_2 = 39.8\gamma_1 \qquad [GHz] \tag{28}$$

$$\Theta = 300/T \tag{29}$$

cloud	class	LWC $[g/m^3]$	altitude [km]	description
stratus	St	0.09—0.9	0—2	Evenly gray, low layer cloud, which causes fog or fine precipitation.
nimbostratus	Ns	0.05—0.65	0—3	Rain cloud. Gray, dark layer cloud, indistinct outlines.
altostratus	As	<0.01—1	2—7	Dense, gray layer cloud, often evenly and opaquely, which lets the sun shine through only a little.
stratocumulus	Sc	<0.1—1	0—2	Cloud plaices, rollers or banks compound dark gray layer cloud.
cumulus	Cu	0.26—1	0—1	Heap cloud with flat basis in the middle or lower level, whose vertical development reminds of the form of towers, cauliflower or cotton.
cumulonimbus	Cb	0.1—2.5	2—23	In the middle or lower level developing thundercloud, which mostly up-rises into the upper level.

Table 2: Liquid water content (LWC) for the principal cloud classes [5].

3.3 Oxygen Absorption

Electric and magnetic dipole transitions are both possible, but magnetic dipoles are weaker and, therefore, not relevant in atmospheric radiative transfer models [5]. An exception to this rule is the superimposition of oxygen magnetic dipole transitions, which generate a strong absorption near 60 GHz.
The oxygen molecule absorption coefficient for the standard atmosphere may be expressed as [7]

$$\kappa_{O_2}(\nu) = 1.6110^{-2}\nu^2 \left(\frac{P}{1013}\right)\left(\frac{300}{T}\right)^2 \mathcal{F}_{O_2}(\nu,\nu_i) \qquad [dB/km] \tag{30}$$

The line shape is given by

$$\mathcal{F}_{O_2}(\nu,\nu_i) = \frac{0.7\gamma_b}{\nu^2+\gamma_b^2} \sum_{j=1,j_m(jodd)} \Phi_j[g_{j^+}(\nu) + g_{j^+}(-\nu) + g_{j^-}(\nu) + g_{j^-}(-\nu)] \tag{31}$$

$$\Phi_j = 4.610^{-3}\left(\frac{300}{T}\right)(2j+1)e^{-6.8910^{-3}\left(\frac{300}{T}\right)j(j+1)} \tag{32}$$

$$g_{j\pm} = \frac{\gamma_j d_{j\pm}^2 + P(\nu-\nu_{j\pm})Y_{j\pm}}{(\nu-\nu_{j\pm})^2+\gamma_j^2} \tag{33}$$

Φ_j represents the fractional population of the line at a given frequency, instead γ_j and γ_b, defined as

$$\gamma_j = 1.18\left(\frac{P}{1013}\right)\left(\frac{300}{T}\right)^{0.85} \qquad \gamma_b = 0.49\left(\frac{P}{1013}\right)\left(\frac{300}{T}\right)^{0.89} \tag{34}$$

represent the resonant and the non-resonant line-width parameters respectively. The line amplitudes d_{j^+} and d_{j^-} are given by

$$d_{j^+} = \left[\frac{j(2j+3)}{(j+1)(2j+1)}\right]^{1/2} \qquad d_{j^-} = \left[\frac{(j+1)(2j-1)}{j(2j+1)}\right]^{1/2} \tag{35}$$

and the O_2 parameters are listed in Tab. 3.

3.4 Integrated Water Vapor

The integrated water vapor (IWV) is an useful tool to infer the atmosphere status. Microwave radiometers, geodetic GPSs (IWV is $\sim 0.5\%$ of total path delay) and radiosoundings are able to provide reliable IWV real-time measurements, while state-of-arts weather models may provide forecasted IWV with a RMS accuracy

j	ν_j^+ [GHz]	ν_j^- [GHz]	$Y_j^+[10^{-4}mbar^-1]$	$Y_j^-[10^{-4}mbar^{-1}]$
1	56.2648	118.7503	4.51	-0.214
3	58.4466	62.4863	4.94	-3.780
5	59.5920	60.3061	3.52	-3.920
7	60.4348	59.1642	1.86	-2.680
9	61.1506	58.3239	0.33	-1.130
11	61.8002	57.6125	-1.03	0.344
13	62.4112	56.9682	-2.23	1.650
15	62.9980	56.3634	-3.32	2.840
17	63.5685	55.7838	-4.32	3.910
19	64.1278	55.2214	-5.26	4.930
21	64.6789	54.6711	-6.13	5.840
23	65.2241	54.1300	-6.99	6.760
25	65.7647	53.5957	-7.74	7.550
27	66.3020	53.0668	-8.61	8.470
29	66.8367	52.5422	-9.11	9.010
31	67.3694	52.0212	-10.30	10.300
33	67.9007	51.5030	-9.87	9.860
35	68.4308	50.9873	-13.20	13.30
37	68.9601	50.4736	-7.07	7.010
39	69.4887	49.9618	-25.8	26.400

Table 3: Rosenkranz O_2 model parameters [8].

of 3 mm [9]. IWV, expressed in mm or equivalently in kg/m^2, is defined as

$$IWV = \int_0^{s_o} \rho_v(s)\, ds \qquad [kg/m^2] \tag{36}$$

where $\rho_v(s)$ is the water vapor density at the height s, which may be expressed as in [10]

$$\rho_v(s) = 2.167\ 10^{-3} \frac{100e(s)}{T(s)} \qquad [kg/m^3] \tag{37}$$

$e(s)$ $[hPa]$ is the water vapor partial pressure. The vapor pressure $e(s)$ may be estimated from the relative humidity definition

$$e(s) = \frac{RH(s)}{100} e_s(s) \qquad [hPa] \tag{38}$$

where $RH(s)$ is the relative humidity in percent at the height s and $e_s(s)$ is the saturation water vapor pressure defined by [11]

$$e_s(s) = 6.1078\ e^{\frac{17.2693882\ T'(s)}{T'(s)+237.29}} \qquad [hPa] \tag{39}$$

where the temperature $T'(s)$ is expressed in ^oC.

3.5 Integrated Liquid Water

GPSs and radiosoundings don't detect the integrated liquid water (ILW), while radiometers and weather models can estimate it. In clear sky conditions ILW is small or nil and becomes significant in presence of cloud cover. The effect of hydrometeors on microwave absorption is relatively weak if referred to water vapor absorption, but for some specific cloud types (e.g. St, Cu and Cb) ILW, and consequently the hydrometeor opacity, drastically increases. ILW is the column integrated amount of liquid droplets forming the clouds defined by

$$ILW = \int_0^{s_o} LWC(s)\, ds \qquad [kg/m^2] \tag{40}$$

where $LWC(s)$[6] at the height s may be calculated as

$$LWC(s) = \rho_a(s) LMR(s) \qquad [kg/m^3] \tag{41}$$

where ρ_a is the air density and $LMR(s)$ is the cloud liquid water mixing ratio $[kg/kg]$ which by definition represents a density ratio. Air density may be derived by [12]

$$\rho_a(s) = 100 \frac{P(s)}{R_d T(s)} \left(1 - \frac{3.78 e(s)}{P(s)}\right) \qquad [kg/m^3] \tag{42}$$

where R_d=287.06 $JKg^{-1}K^{-1}$ is the specific gas constant. P is the pressure and $e(s)$ is the vapor partial pressure (both in hPa).

4 Weather Forecast Model

The weather model we use is managed by ARPAS, that daily provides Osservatorio Astronomico di Cagliari (OAC) with the outputs of the Weather Research and Forecasting nonhydrostatic mesoscale model (WRF-NMM) [9]. The WRF-NMM model is a state-of-the-art numerical weather prediction system developed by a collaboration between the National Center for Atmospheric Researchs (NCAR) Mesoscale and Microscale Meteorology (MMM) Division, the National Oceanic and Atmospheric Administrations (NOAA) National Centers for Environmental Prediction (NCEP).
The model requires initial and boundary conditions being input at appropriate time intervals. Moreover, a representation of the orography, land use and surface roughness is needed to calculate the forces acting near the surface. The initial and boundary conditions arise from the outputs of other simulations performed with coarser spatial resolution [13].
The forecast area ranges from 6.9° to 11° E and from 38.3° to 41.6° N, including the Sardinia Island (see Fig. 5), and defining a grid of 217×219 grid points with a spatial resolution of about 2 km. Furthermore, 45 vertical levels above the ground of this area and the 36-hours forecast adopting a 4-seconds time step are usually considered.
However, since each model produces a big dataset, the time resolution and the number of the vertical layers are suitably reduced. Only about 250 MB data are stored in grib format[7] and sent to a server hosted in OAC, where are processed. They includes 13×3-hours epochs (epoch#1=12 UTC) and 19 vertical layers (from 1000 to 100 hPa) and only a few parameters, the most interesting ones for our application. Some of available parameters are listed below:

- 13 forecasts from 12 UTC, time resolution = 3 hr;
- x_{grid} = 217, 6.935° E, step=0.0186°;
- y_{grid} = 219, 38.346° N, step=0.0150°;
- 19 pressure levels: 1000 950 900 850 800 750 700 650 600 550 500 450 400 350 300 250 200 150 100, [hPa];
- Surface Total precipitation (APCPsfc), $[kg/m^2]$;
- Dew point temp. profile, 19 layers, (DPTprs), [K];
- Geopotential height profile, 19 layers, (HGTprs), [m];
- Column Total cloud cover (TCDCclm), [%];
- Relative humidity profile, 19 layers, (RHprs), [%];

[6] Note that LWC is the same observable previosly introduced in the absorption coefficient definition, in this case expressed in Kg/m^3.

[7] http://www.cpc.ncep.noaa.gov/products/wesley/wgrib.html

- Surface Snow depth (SNODsfc), [m];
- Temperature profile, 19 layers, (TMPprs), [K];
- u wind component 10 m above ground (UGRD10m), [m/s];
- v wind component 10 m above ground (VGRD10m), [m/s];
- Cloud water mixing ratio profile, 19 layers, (CLWMRprs), [kg/kg].

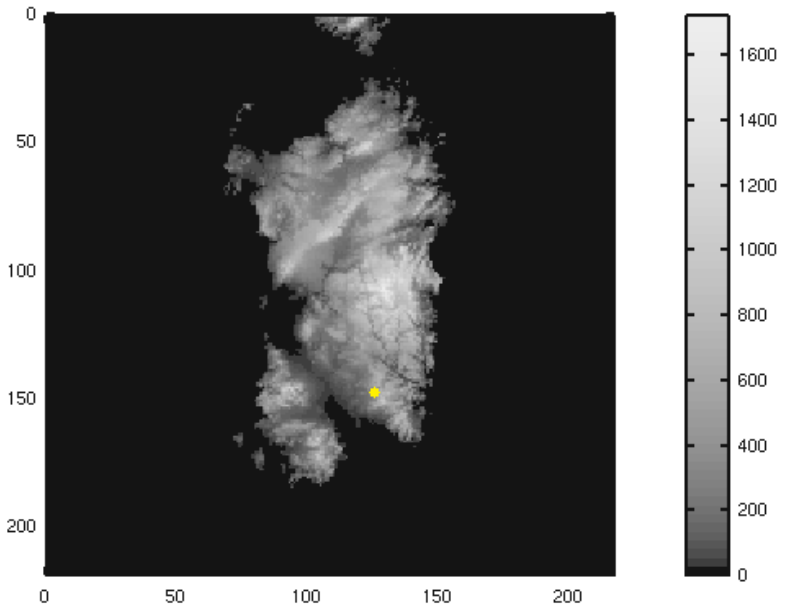

Figure 5: Model forecast area: 19 vertical layers are provided for the grid of 217×219 points, the yellow dot indicates the SRT site position (the image represents the orography, height a.s.l. [m]).

The cloud water mixing ratio (which is closely related to the LWC) has been added to the grib archives since May 2015, allowing to predict the cloud cover (liquid water) effects.
The antenna temperature, the integrated water vapor, the sky opacity, etc. are derived from these parameters, providing useful information for the scheduling of the antenna activities. Furthermore, model outputs such as wind speed, the total precipitation and the snow depth may be employed for the antenna safety.

5 T_{SYS} Forecast Procedure Test

This section presents tests to verify the T_{SYS} forecast procedure. First, a comparison between the three outputs of the procedure, see Fig. 1, and a SRT skydip data set performed in 2014 with the K-band multibeam receiver, is discussed in Section 5.1. In Section 5.2 a WRF-NMM prediction of the SRT atmosphere opacity has been checked with the opacity value measured during a SRT K-band survey. Finally, in Sections 5.3 and 5.4 two examples of how the weather model is able predict the opacity, even when sudden atmospheric phenomema occur, are shown.

5.1 2014 Skydip Dataset

In order to assess the procedure in a realistic case, T_{SYS}^{WRF}, T_{SYS}^{RDS}, calculated in (1) by using respectively the WRF and RDS data, and T_{SYS}^{RDM} in (10) exploiting the RDM data, have been compared with T_{SYS}^{SRT} available at the SRT data archive, related to the K-band multi-feed skydip series recorded in 2014. It is worth noting that in (1) T_{REC} has been chosen equal to 35 K, i.e. the worst value of the receiver temperature at 22 GHz measured during the receiver test performed at the Medicina laboratory of the Istituto di Radio Astronomia [14].
The comparison between T_{SYS}^{SRT}, measured at 22 GHz and at an elevation angle equal to 70°, and the other system temperatures is summirazed in Fig. 6 and in Tab. 4. In most the epochs (from 1 to 12 and from 21 to 22) listed in the second column of Tab. 4 one can note a very good agreement between T_{SYS}^{SRT} and T_{SYS}^{RDM} with a maximum percentage difference of about 3%, which becomes 7% and then got worse up to 17%, after comparing T_{SYS}^{SRT} to T_{SYS}^{WRF} and T_{SYS}^{RDS} respectively. Unfortunately two RDS launches per day are not enough to get a better agreement between T_{SYS}^{SRT} and T_{SYS}^{RDS}.
Actually, something different occured in the epochs from 13 to 20 corresponding to the November 20 and 21 nighttime measurements. During these experiments the T_{SYS}^{SRT} turned out to be higher (even up to 40 K larger) than the T_{SYS}^{SRT} measured in the epochs from 1 to 12 and from 21 to 22. On the contrary T_{SYS}^{RDM}, T_{SYS}^{WRF}, and T_{SYS}^{RDS} kept the same trend for all the epochs considered. In Fig. 6, one can better see how the T_{SYS}^{SRT} values differ from the T_{SYS}^{RDM} when that unexpected behaviour occured.
A deep investigation to figure out what happened during the epochs from 13 to 20 was carried out by retrieving all the available weather data. Although the antenna logbook recorded a clear sky, no fog, no clouds and weak wind condition, the ground weather station measured a relative air humidity very close to saturation point (the dew-point was close to the actual air temperature). In this case, the moisture may condensate and liquid water may accumulate on some (critical) parts of the antenna, for instance on the vertex-room hole window. The same anomaly has been previously reported during the early K-band multi-feed receiver calibration surveys [15] and, more recently, during an accurate calibration campaign [16].

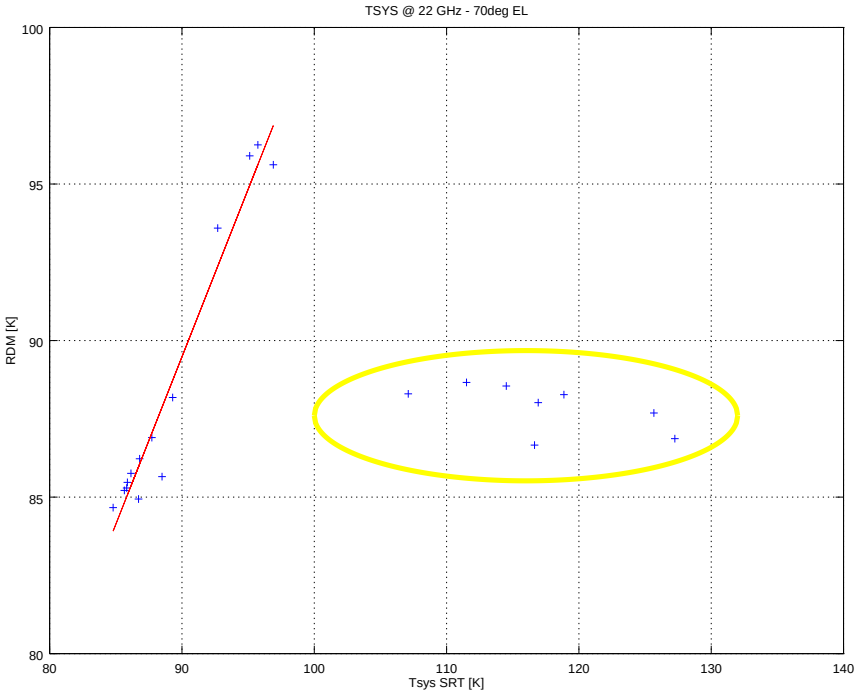

Figure 6: T_{SYS}^{SRT} vs T_{SYS}^{RDM} scatter plot, the clustered data in the yellow circle are the outliers due to liquid water condensation on the antenna surface.

N	Epoch	freq.[GHz]	T_{SYS}^{SRT} [K]	T_{SYS}^{RDM} [K]	T_{SYS}^{WRF} [K]	T_{SYS}^{RDS} [K]	T_{REC}^{*} [K]
1	09/26/14 - 07:59:00 AM	21.7	85.9	85.5	82.2	79.9	38.7
2	09/26/14 - 08:50:00 AM	21.7	86.7	84.9	82.2	79.9	39.5
3	09/26/14 - 09:49:00 AM	21.7	87.7	86.9	82.2	79.9	40.5
4	09/26/14 - 10:42:00 AM	21.7	89.3	88.2	88.6	79.9	35.7
5	09/26/14 - 12:56:00 PM	21.7	92.7	93.6	88.6	79.9	39.1
6	09/26/14 - 01:50:00 PM	21.7	96.9	95.6	101.2	79.9	30.7
7	11/01/14 - 12:06:00 AM	21.7	84.8	84.7	82.2	81.5	37.6
8	11/01/14 - 12:59:00 AM	21.7	85.6	85.2	82.2	81.5	38.4
9	11/01/14 - 01:52:00 AM	21.7	85.8	85.3	82.7	81.5	38.1
10	11/01/14 - 02:44:00 AM	21.7	86.8	86.2	82.7	81.5	39.1
11	11/01/14 - 03:36:00 AM	21.7	86.1	85.8	82.7	81.5	38.4
12	11/01/14 - 04:28:00 AM	21.7	88.5	85.6	82.7	81.5	40.8
13	11/20/14 - 11:14:00 PM	21.7	**116.6**	86.7	86.2	88.0	65.4
14	11/20/14 - 11:57:00 PM	21.7	**127.3**	86.9	86.2	88.0	71.8
15	11/21/14 - 12:40:00 AM	21.7	**125.7**	87.7	88.9	88.0	63.2
16	11/21/14 - 01:22:00 AM	21.7	**118.9**	88.3	88.9	88.0	60.8
17	11/21/14 - 02:04:00 AM	21.7	**116.9**	88.0	88.7	88.0	57.8
18	11/21/14 - 02:46:00 AM	21.7	**114.5**	88.5	88.7	88.0	53.4
19	11/21/14 - 03:27:00 AM	21.7	**111.5**	88.7	88.7	88.0	31.6
20	11/21/14 - 04:10:00 AM	21.7	**107.1**	88.3	88.7	88.0	31.0
21	12/19/14 - 12:37:00 PM	22.1	95.7	96.3	99.1	94.0	34.4
22	12/19/14 - 12:52:00 PM	22.1	95.1	95.9	99.1	94.0	34.2

Table 4: Antenna system temperature (T_{SYS}^{SRT}) at elevation equal to 70° compared with the radiometer, the numerical weather model and radiosoudings (T_{SYS}^{RDM}, T_{SYS}^{WRF} and T_{SYS}^{RDS} respectively). Note that the time resolution (two launches per day) of the radiosoundings is too coarse to describe the high variability of atmospheric phenomena. The bold text emphasizes the abnormal T_{SYS}^{SRT} values observed nighttime November 20 and 21. T_{REC}^{*} is an estimate of receiver temperature (see text).

In addition, the last column of Tab. 4 (T_{REC}^{*}) merely reports the difference between the T_{SYS}^{SRT} and T_{SYS}^{*RDM}, where the latter is the system temperature as measured by the radiometer without adding the assumed T_{REC} of 35 K. T_{REC}^{*} is thus a "measured" receiver temperature, whose average value, about 38 K, is greater than T_{REC} of about 3 K. This additional and unexpected contribution is still "unexplained". Obviously, in those anomalous cases, in which the T_{SYS}^{SRT} strongly deviates from the expected values, even T_{REC}^{*} turned to be quite different and it lost its meaning.

5.2 K-band Survey

During the aforementioned multi-feed calibration survey [16], the reliability of the procedure has been tested again, trying to guess several hours in advance the atmosphere opacity. The 36-hour forecast (one every 3 hours with a total 13 issues) of the opacity issued at 12 a.m. on July 6 2015, and a 23 GHz skydip performed in the early evening of the same day are respectively shown in the top and bottom panel of Fig. 7. The sudden decreasing of the opacity (from 0.17 to 0.145) was predicted between 12 p.m. and 9 p.m. on July 6, as well as the opacity value of about 0.15 around 8 p.m. (top panel in Fig. 7). The predicted value is in good agreement with that measured with the skydip preformed nearly at the same time ($\tau = 0.155$), see bottom panel in Fig. 7.

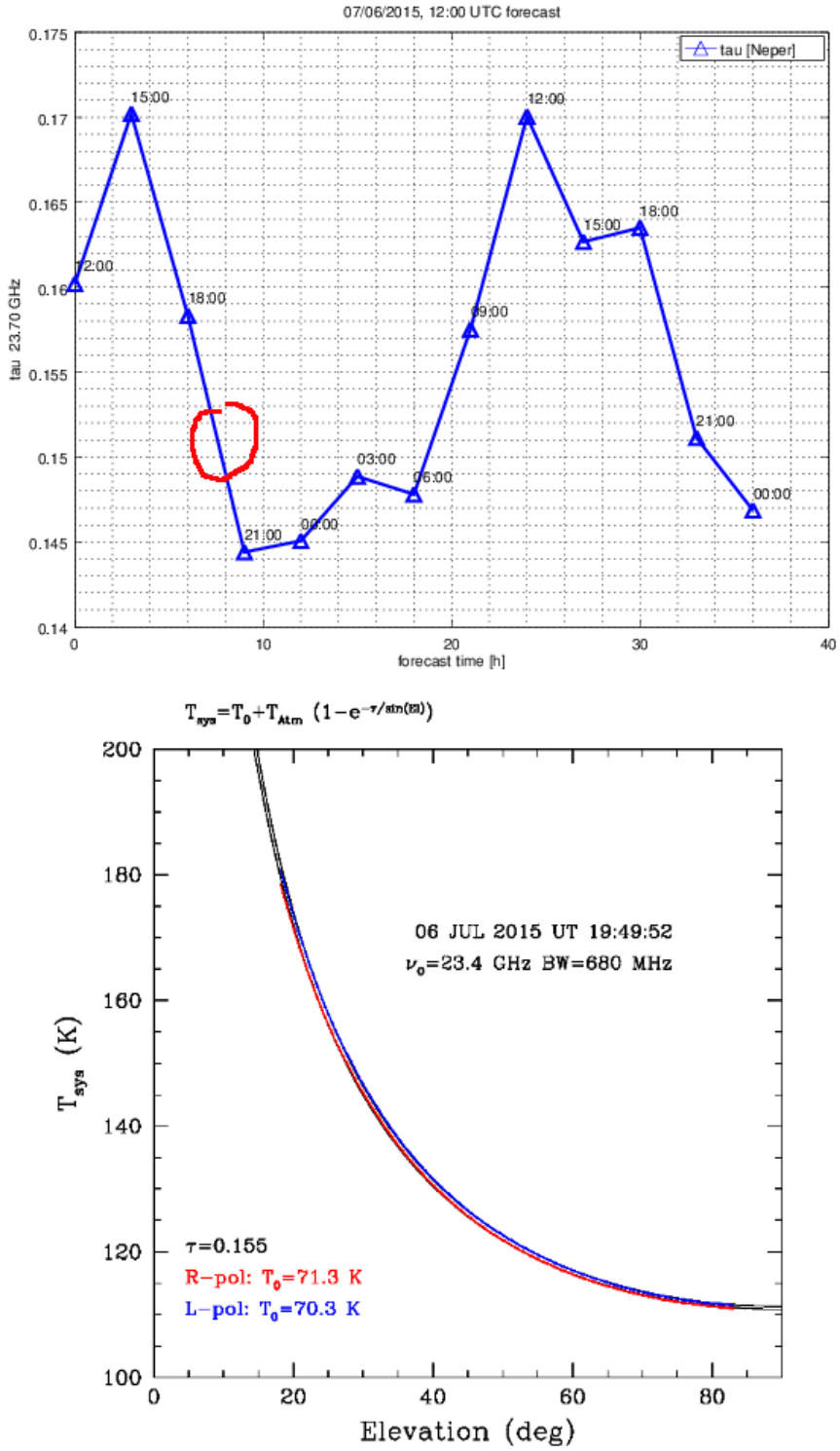

Figure 7: Example of the model use in operative conditions: predicted (top) and measured (bottom) opacity. The bottom panel is the measured T_{SYS} versus elevation. A fit of (10) gives an indipendent estimate of τ (courtesy of Matteo Murgia).

5.3 Wind "Cleaning" Effect

The availability at the SRT site of a radiometer allows one to locally check the reliability of the WRF-NMM model forecast, for example, when a unusual atmosphere scenario is predicted, see Fig. 8. With this purpose, in Fig. 8 a screen shot of the SRT radiometer application, taken on July 9 (left panel) and a 36-hour forecast of the atmosphere opacity at 22 GHz, issued on July 8 (right panel), are compared. The forecast was that an "atmospheric window" characterized by a sudden and significant decrease of the opacity with a minimum value equal to 0.07 Neper would have occured at 9 a.m. UTC. As one can read in the screen shot, the prediction was confirmed by the radiometer, which at 8:32 a.m. UTC measured an opacity (tau) at 22 GHz almost equal to the predicted one. In this case the opacity decreasing was likely caused by the injection of "clean" air carried by north-westerly winds, as the SRT weather station reported. In fact, the Mistral unexpectedly brought the opacity to winter-like values. At 22 GHz such an opacity value close to 0.07 Np is not frequent in summer at SRT, occurring with a probability of about 10% [4].

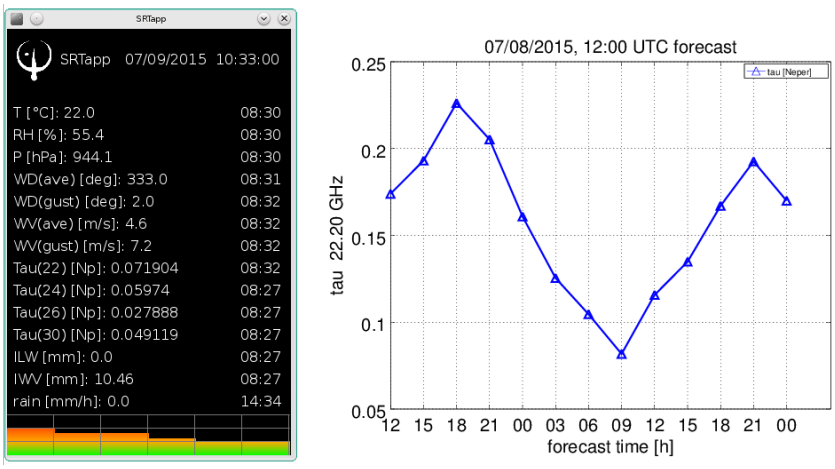

Figure 8: Comparison between the atmosphere opacity measured by the radiometer (on the left a screen shot of the SRT radiometer application) and forecasted by the WRF-NMM model (on the right a tau forecast time plot).

5.4 Late Spring Storm

In this section another example of how the procedure may be useful to predict a typical late spring/early summer weather instability is presented. The meteorological framework on June 16-17 2015 was characterized by strong variability, alternating clear sky with cloudy cover or heavy rain. Fig. 9 shows WVC and LWC vertical profiles for two forecasted epochs: epoch#1 corresponding to 12:00 UTC on June 16 and epoch#6 corresponding to 03:00 UTC on June 17 (remember that each model issue consists of 13 epochs covering 36 hours).
Fig. 10 shows the 22 GHz opacity behavior during the 36 hours considered by the forecast. The opacity drops from 0.24 to 0.14 Neper in 15 hours (from 12 p.m. to 3 a.m.), but it is worth noting that the optimal atmosphere configuration (from radio astronomical point of view) is reached at epoch#6, when a thick cloud system was sitting over the SRT site (Fig. 10, epoch#6, i.e. at 3:00 A.M. UTC). It is evident that the good opacity value reached in epoch#6 is due to the strong decrease in WVC. In this case, the rule-of-thumb approach of considering the clear sky as the best choice for high frequency astronomical observations may be misleading.

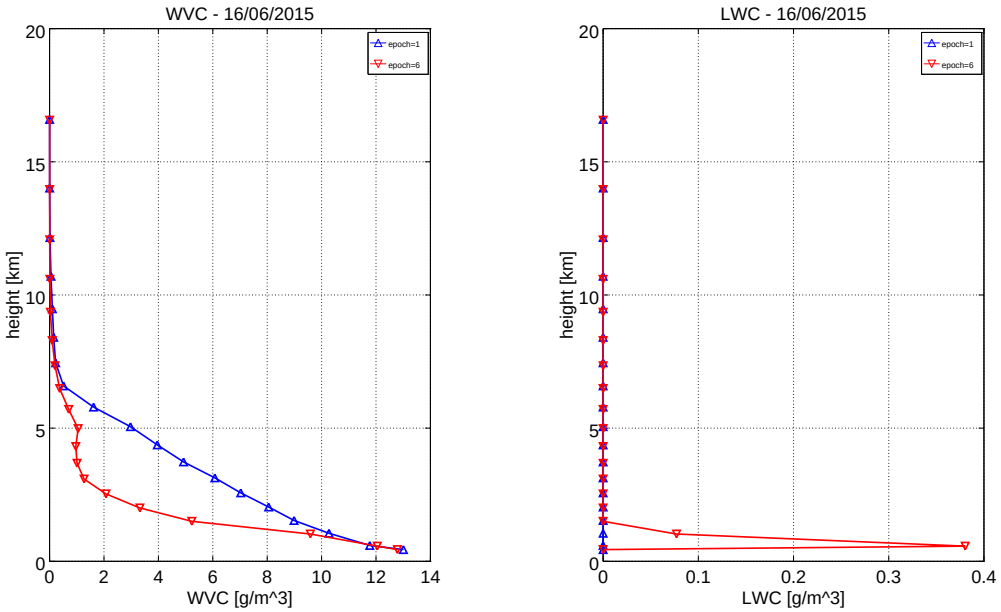

Figure 9: Forecasted water vapor profiles (left) and forecasted liquid water profiles (right) for epoch#1 (12:00 UTC on June 16) and epoch#6 (03:00 UTC on June 17), note that for epoch#1 cloud cover was absent, while for epoch#6 low-layer-clouds were present (LWC$\sim$ 0.4 g/m^3).

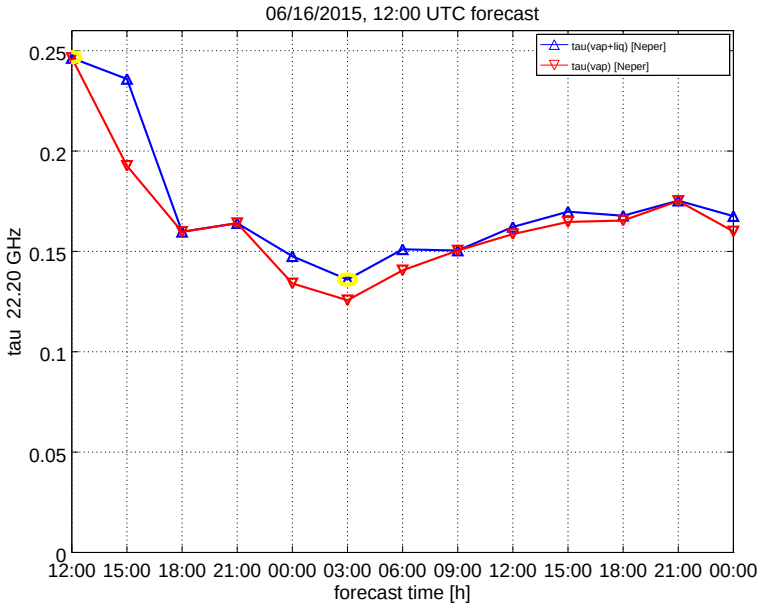

Figure 10: Forecasted 22 GHz opacity (τ) for June 06-07 2015 (yellow circles indicate epoch#1 and epoch#6). In epoch#6 the sky opacity was lower although the cloudy/rainy conditions (the opacity is modeled with and without the LWC contribution). The liquid contribution to opacity is, in this case, less than 10%.

6 Conclusions

Nowadays, modern radio astronomical facilities like SRT are designed with frequency agility capability. This means, in principle, that the telescope schedule could be dynamically arranged in function of the environmental conditions with the aim to match the atmospheric transparency with the astronomer proposal. This strategy may become a strong constraint for the high frequency observation proposal.
A rigorous procedure for the SRT T_{SYS} prediction based on a dynamic approach has been presented. As described in the previous sections, on the one hand, RDS and WRF data can be used to calculate T_{SYS}, but only the WRF-NMM model allows one to forecast an atmosphere scenario 36 hours in advance with a time resolution of 3 hours. On the other hand, the RDM data allows one a real-time monitoring of the atmosphere opacity and, thus, of the SRT T_{SYS}. In the presented cases, the comparison with skydip measurements showed that SRT T_{SYS} can be monitored in real-time with a maximum error of 3% with RDM data, and we can predict it up 36 hours in advance with a maximum error of 7% using the WRF model. In the worst cases, when the weather phenomena significantly vary in a time scale less than 3 hours, i.e. the time resolution of the WRF-NMM model, the weather parameters can be provided by the radiometer and the other meteorological sensors available at the SRT site. In effects, such data can be added to the model information in order to return a more accurate prediction.
Also, one must not forget that the weather models can be used for the antenna safety and its pointing efficiency. In fact the strong wind may make worse the antenna pointing accuracy and, in extreme conditions, may cause the antenna stop.
Finally, it is worth pointing that, after this preliminary phase, in which calibration and validation are still in progress, two improvements can be still added to the procedure: first implementing an accurate calculation of η_f by fitting several SRT skydip data set; then providing the SRT users with Graphic User Interface to retrieve easily the forecasted and monitored atmosphere data in a simple and efficient way.

Acknowledgements

The authors are grateful to dr Simona Righini for providing us with the SRT skydip data.

This project has been supported by MIUR, PRIN 2010-2011, “Tecniche geomatiche innovative ed emergenti di rilievo, telerilevamento (da aereo, satellite, uav) e WEBGIS per la mappatura del rischio in tempo reale e la prevenzione del danno ambientale”.

References

1. Cortés Medellín, G., “Antenna Noise Temperature Calculation”, US-SKA Technical Memo Series, Memo 95.
2. Bolli, P., et al., “Basic Element for Square Kilometer Array Training (BEST): Evaluation of the Antenna Noise Temperature”, IEEE Ant. Prop. Magazine, 50(2), 58, 2008.
3. Wilson, T.L., et al., “Tools of Radio Astronomy”, 5th edn., Astronomy and Astrophysics Library. Springer, Berlin, 2009.
4. Nasir, F.T., et al., “Atmospheric Conditions at the SRT Site”, OAC Int. Rep., 16, 2011.
5. Eriksson, P. and Buehler, S., “ARTS User Guide”, http://www.sat.ltu.se/arts/docs/.
6. Ulaby, F.T., et al., “Microwave Remote Sensing”, Vol I, Addison-Wesley Publishing Company, ch. 4-5, 1981.
7. Rosenkranz, P., “Shape of the 5 mm Oxygen Band in the Atmosphere”, IEEE Trans. Antennas and Propagation, 23(4), 498, 1975.
8. Liebe, H.J. , et al., “Propagation modeling of moist air and suspended water/ice particles at frequencies below 1000 GHz”, Proc. NATO/AGARD Wave Propagation Panel, 52nd meeting, No. 3/1-10, Mallorca, Spain, 17 - 20 May, 1993.

9. Nasir, F.T., et al., "Weather Forecasting and Dynamic Scheduling for a Modern cm/mm Wave Radiotelescope", Exp. Astron., 36(1/2), 407, 2013.

10. Liu, Y., "Precision of Precipitable Water Vapor from Radiosonde Data for GPS Solutions", Geomatica, 54(2), 171, 2000.

11. Varmaghani, A., "An Analytical Formula for Potential Water Vapor in an Atmosphere of Constant Lapse Rate", Terr. Atmos. Ocean. Sci., 23(1), 17, 2012.

12. Brutsaert, W., "Evaporation into the Atmosphere: Theory, History and Applications", Dordrecht, Holland Reidel, 1982.

13. http://www.sar.sardegna.it/documentazione/meteo/modelli.asp

14. Orfei, A., et al., "A Multifeed Receiver in the 18-26.5 GHz Band for Radioastronomy", IEEE Ant. Prop. Magazine, 52(4), 62, 2010.

15. Orfei, A., "Test di Stabilità e Temperatura di Sistema del Ricevitore 22 GHz in Fuoco Gregoriano", SRT Tech. Mem., SRT-TES-10000-002-01, 2012.

16. Righini, S., Private Communication.